science.sciencemag.org/cgi/content/full/science.aay3705/DC1

Supplementary Materials for

Color, composition, and thermal environment of Kuiper Belt object (486958) Arrokoth

W. M. Grundy*, M. K. Bird, D. T. Britt, J. C. Cook, D. P. Cruikshank, C. J. A. Howett, S. Krijt, I. R. Linscott, C. B. Olkin, A. H. Parker, S. Protopapa, M. Ruaud, O. M. Umurhan, L. A. Young, C. M. Dalle Ore, J. J. Kavelaars, J. T. Keane, Y. J. Pendleton, S. B. Porter, F. Scipioni, J. R. Spencer, S. A. Stern, A. J. Verbiscer, H. A. Weaver, R. P. Binzel, M. W. Buie, B. J. Buratti, A. Cheng, A. M. Earle, H. A. Elliott, L. Gabasova, G. R. Gladstone, M. E. Hill, M. Horanyi, D. E. Jennings, A. W. Lunsford, D. J. McComas, W. B. McKinnon, R. L. McNutt Jr., J. M. Moore, J. W. Parker, E. Quirico, D. C. Reuter, P. M. Schenk, B. Schmitt, M. R. Showalter, K. N. Singer, G. E. Weigle II, A. M. Zangari

*Corresponding author. Email: w.grundy@lowell.edu

Published 13 February 2020 on *Science* First Release
DOI: 10.1126/science.aay3705

This PDF file includes:

Other supplementary material for this manuscript includes:

Data S1 (.obj file)

Materials and Methods

Ralph Instrument Details and Data Processing

The Ralph instrument is a three-mirror anastigmat telescope with a dichroic beamsplitter that feeds two focal planes, making it effectively two instruments in one *(14)*. The MVIC focal plane consists of 6 time delay integration (TDI) charge-coupled device (CCD) arrays and one frame transfer CCD. The TDI detectors have 32 rows to build up the integrated signal as the instrument scans the field of view across the scene. In the cross-track direction, orthogonal to the 32 TDI lines, there are 5000 active pixels. Each pixel subtends 20 μrad for a cross-track field of view of 5.7°. Ralph/MVIC is distinguished from other New Horizons imaging instruments for its wide field of view and color imaging capabilities. Four of the 6 TDI detectors have broadband filters fixed to the detector assembly. The color filters are identified as "BLUE" (400-550 nm), "RED" (540-700 nm), "NIR" (780-975 nm) and "CH4" (860-910 nm). The two Panchromatic TDI detectors cover the wavelength range from 400-975 nm; see *(89)* for details of system response and calibration. Comparing the observed signal for a well lit portion of Arrokoth to the standard deviation in a sample of blank sky, we estimate the single pixel signal-to-noise ratios to be 60, 175, 148, and 57 in BLUE, RED, NIR, and CH4 filters, respectively. The corresponding 1-σ uncertainty in a percent color slope measurement is about ±0.2 around the mean slope of 27%. The uncertainty in determination of a mean color slope drops rapidly as multiple pixels are averaged together.

Ralph's LEISA focal plane consists of a Rockwell Scientific Corporation PICNIC array (a 256×256 pixel HgCdTe device) with two linear variable filters to disperse the light. The larger filter covers wavelengths from 1.25 to 2.5 μm with a resolving power ($\lambda/\Delta\lambda$, where λ is the wavelength) of ~240. The smaller filter covers 2.1 to 2.25 μm with a higher resolving power (~560). The LEISA detector has a field of view of 0.9° with both axes providing spatial data coupled with spectral dispersion along one axis.

For all the data collecting modes of Ralph (except observing with the panchromatic frame transfer array), the spacecraft scans the Ralph boresight across the target to build up an image or image cube in the case of LEISA. At Arrokoth, our scan rates were slower than previously used at Pluto because of the low light levels at Arrokoth's extreme distance from the Sun (43 au at the

time of the encounter) and its low albedo. The color scans used a commanded rate of approximately 800 μrad s^{-1} which corresponds to an integration time of 0.8 seconds. The instrument reads the actual scan rate of the spacecraft to set the TDI rate or frame rate for data collection: the actual scan rate is within ±32 μrad s^{-1} of the commanded scan rate. For the LEISA observations, we used a very slow scan rate (60 μrad s^{-1}) to maximize the observed signal.

We used three LEISA scans of Charon taken during the Pluto encounter to construct a flat field for LEISA. Charon was used for this purpose because of the lack of spectral diversity across its surface, unlike Pluto. The three highest spatial resolution scans of Charon *(90)* were used in order to check for consistency. These are identified as C_LEISA_HIRES, C_LEISA_LORRI and C_LEISA. In each of these scans, Charon passed through the center of the field-of-view with the C_LEISA_HIRES scan subtending the greatest area of the detector. Charon did not completely fill the detector in any of these scans, so there are regions around the frame edges which have not been corrected, but Arrokoth was not imaged in these uncorrected regions.

Using the frame data (spatial vs. spatial-spectral format), a mask was constructed to isolate Charon from the background. The average signal was then calculated for each pixel when it was illuminated by Charon. This produced a 256×256 pixel array (with pixels set to zero if never illuminated by Charon) with the mean spectrum of Charon still present. That was removed by robust fitting (i.e., with rejection of outlier points) of a single-order polynomial to each row (wavelength) of the frame. The results from each of the Charon scans were then combined where they overlap. The result is the ratio of the new flat to the old flat with which the Charon data had already been processed by the standard pipeline. After multiplying by the old flat, the new flat was obtained.

To extract the spatially-registered spectra of Arrokoth from the LEISA data frames, a frame-by-frame pointing solution was determined. The changing spacecraft-to-target range during the LEISA scan resulted in a spatial scale that changed from 2.0 to 1.8 km/pixel over the time the scan, with the closer range coinciding with longer wavelengths. The range was taken from predicted SPICE *(91)* kernels for the observation time of each frame, and used to construct a scaled model image of Arrokoth (two sky-plane circles connected by a rectangular neck). The

focal plane center of figure, mean albedo, and the full width at half maximum of a Gaussian point spread function was varied until the mean squared difference between a given frame and the model was minimized. Parameter optimization was achieved with simplex minimization. The position angle of the neck and two spheres was assumed to be fixed in all frames. In the case where a pointing solution failed (such as when the target was crossing the edge of the focal plane), the position was estimated via linear interpolation from the nearest successful solutions.

Pixel coordinates in each plane were then converted into a physical frame relative to the center of figure using the range prediction. The (Δx (km), Δy (km), λ (μm)) coordinates of each pixel were stored, where Δx and Δy are distance from the center of figure along the axes of the detector array, along with the I/F measured by that pixel. A mask of hot pixels and cosmic rays was applied at this stage, and flagged pixels were removed from this data structure. A nearest-neighbor interpolant was constructed to interpolate these I/F measurements over these coordinates. The final spectral cube was constructed by constructing a (Δx, Δy, I/F) plane from this interpolant sampled over a spatially-uniform grid sampled at 10 times the average native spatial resolution at each unique wavelength sampled by the measurements.

Spectral Modeling

Multiple scattering of incident sunlight by a granular surface as a function of composition and texture was simulated using a Hapke model *(31, 92)*. This model was numerically inverted to obtain the best-fitting representations of surface composition and texture, given a set of assumed ingredients and parameters. Because there is an infinite set of potential ingredients and parameters, the resulting best-fitting representations are necessarily not unique solutions, though they can demonstrate that a particular configuration is consistent with the data, and assess spectral differences between regions. Although the MVIC data could provide additional constraints, the models are only applied to LEISA data, because the MVIC and LEISA data sets were obtained at different times and thus at different viewing geometries.

For Hapke parameters, we assumed the single scattering phase function, $P(g)$, from *(3)*, characterized by McGuire & Hapke parameters $b = 0.3178$ and $c = 0.7450$ *(93)*. Hapke's opposition effect and macroscopic roughness parameters were not used (by setting Hapke's B_0 and $\bar{\theta}$ parameters to zero). Because all of the spectra being modeled were averages over a range of incidence and emission angles, we computed the models for simplified geometry with incident

angle i = 30°, emission angle e = 30°, and phase angle g = 10°. These simplifications are justified by the low signal-to-noise ratio of the data and the coarseness of the spatial registration of the data, owing to the complex shape of the body and changing geometry from spacecraft motion during the LEISA scan. The target was in LEISA's field of view for a little over 4 minutes, during which the spacecraft closed from 32,770 to 29,110 km range from Arrokoth. The changing range is accounted for in our processing of LEISA data, but the phase angle also changed during the scan, and this change is not accounted for. During the scan, the phase angle grew from 12.49° to 12.79°. The start of the scan corresponds to the short wavelength end of the spectral range, so not accounting for this change in geometry could introduce a spurious spectral slope, but with just a 0.3° change over LEISA's spectral range, this is a small effect. This changing geometry over time also results in slightly different geometry between the LEISA data and the LORRI rider obtained during the same scan (see *(3)*, their table S1).

We fitted models to the grand average spectrum incorporating a variety of potential ingredients. We considered the Akaike and Bayesian information criteria (AIC and BIC) to assess whether the inclusion of each particular ingredient was able to reduce χ^2 sufficiently to justify its inclusion. We found only five ingredients to be statistically supported on this basis: tholin, amorphous carbon, and CH_3OH ice, with this model accounting for 92% of the marginalized probability according to the AIC, and to a lesser extent, NH_3 ice at 4.5%, and H_2O ice at 3%. According to the BIC, inclusion of H_2O and NH_3 are less supported, because it penalizes the inclusion of additional model complexity more harshly than the AIC. We used optical constants for these materials from *(20, 92, 94-96)* for tholin, CH_3OH ice, amorphous carbon, H_2O ice, and NH_3 ice, respectively. Tholins from a variety of sources were tried, but according to AIC and BIC criteria, no particular tholin is favored. Titan tholin *(20)* should be seen not as a specific identification but as a generic representative of this broad class of materials. Likewise, amorphous carbon *(94)* is a generic dark opaque material, and is not necessarily an exact match for the dark material present on Arrokoth.

REX Data Processing

From the shape model of Arrokoth *(3)*, the projected area of Arrokoth as observed from New Horizons at 05:52:14 UTC (time of minimum separation between the high-gain antenna (HGA) boresight and the position of Arrokoth), was 414.4 km^2. The distance at this time was

16,700 km. The main beam of the HGA at this distance covered an area about 230 times larger than the target, so the REX measurement was unresolved and only a global determination of the Arrokoth brightness temperature is possible. The observed radio flux is therefore a combination of source plus sky background. The contribution of the background was determined by performing an additional scan along the identical path in right ascension and declination, but one day after the flyby. As viewed from the spacecraft (Fig. 6A), Arrokoth was located on the edge of the Galactic plane in the opposite direction from the Galactic Center, well separated from all bright natural radio sources. With imperfect a priori knowledge of the precise location of Arrokoth, the REX scan was designed to cover all possible time-of-flight errors between ±180 seconds of the nominal flyby design. This required scanning the HGA over a lengthy arc of 1.2° in RA and 10.2° in Dec, more than adequate to assure covering the slower motion of Arrokoth on the sky (0.5° in RA; 4.2° in Dec). As it turned out, the target was 23 seconds late and thus near the middle of the pre-planned scan range.

The brightness temperature of the sky background within the HGA beam was determined to be only slightly higher than the cosmic microwave background temperature T_{CMB} = 2.73 K. Nevertheless, the radio flux density from the background in each receiver is still about 25 times stronger than the maximum due to the excess thermal emission from Arrokoth. The main contributor to the observation noise, the system temperature of each receiver (REX A~146 K; REX B~137 K), was assumed to remain constant during each scan.

The flux density recorded for the target scan on encounter day is shown together with the background scan recorded one day later (Fig. 6B). The smooth black curve shows the modeled effect of an unresolved Arrokoth with a brightness temperature of 30 K. The target and background scans are plotted over their common declination interval in order to distinguish possible variations in the background. Both curves show only the changes in flux density with respect to the mean value measured during a calibration interval (also indicated in Fig. 6B), defined as those times when the HGA boresight was well separated from Arrokoth. The plotted flux density is a stacked average of the measurements from the two receivers, REX A and REX B, smoothed over a running interval of 0.75° in declination. The smoothing interval was selected as an optimum value: wide enough to reduce the measurement noise, but still narrow enough to capture changes during the roughly 80 seconds when Arrokoth passed through the HGA beam.

Appropriate for the point source case, the observations were fitted to a model with a Gaussian superimposed on a linear background. The best fitting model yielded a change in flux density at maximum of 62 ± 10 Jansky, where the uncertainty accounts for the standard deviation of the entire fit to the data. Converting this to the global brightness temperature of Arrokoth *(36, 37)* yields T_B = 29 ± 5 K, roughly corresponding to a 6-σ detection. Different declination smoothing intervals from 0.25° to 1.25° led to changes in brightness temperature of less than 1 K.

Thermal models

Our modeling is based on the Arrokoth global shape model *(3)*, reduced to a "low poly" version with N_f = 1962 triangulated facets (Data S1). For a given facet *i*, with surface area σ_i and outward pointing normal vector $\mathbf{n}_i$, we determine which other faces *j* are viewable from it using simple ray-tracing, and from this we develop a logical face network N_{ij}, sometimes referred to as the "who-sees-who" list *(38)*. For each *i*-*j* pair, we assess their relative distance r_{ij} with corresponding unit vector $\mathbf{r}_{ij}$. This procedure is nominally an O(N_f^2) calculation, but is done only once for any given shape model and is subsequently used for all derived thermal models. This methodology accounts for large scale roughness expressed in the faceted shape model, but does not account for smaller scale roughness which can also be expected to affect surface temperatures.

We adopt a surface plus one-dimensional subsurface model to describe the near surface energy balance in which losses to radiation and subsurface conduction is balanced by the net received energy, Φ_i, which is the radiative losses plus the gains from both solar insolation and surface re-radiation,

$$\begin{aligned} k\,\partial_z T_i|_{z=0} + \epsilon_i \sigma_B T_i^4 \;&=\; \Phi_i \;=\; (1-A_i) F_i + \sum\nolimits_j \epsilon_j \sigma_B K_{ij} T_j^4, \\ F_i \;&=\; F_* (\mathbf{n}_* \cdot \mathbf{n}_i), \end{aligned} \tag{S1}$$

where *z* is depth and the summation is over all non-zero N_{ij}. T_i is the surface temperature of element *i*. The local emissivity is ϵ_i (assumed to be 0.9, following *(40, 43)*), F_i is the non-self-blocked insolation received by surface element *i* from the Sun located in the sky by unit vector $\mathbf{n}_*$, $(1-A_i)F_i$ is the absorbed solar radiation flux (taking into account self-shadowing), and A_i the bond albedo, measured to be 0.06 *(1, 3)*. The scaled radiated power emanating from facet *j* and received by facet *i* is quantified by the following expression:

$$K_{ij} \;=\; \sigma_i N_{ij} \frac{(\mathbf{n}_i \cdot \mathbf{r}_{ij})(-\mathbf{n}_j \cdot \mathbf{r}_{ij})}{2\pi r_{ij}^2}. \tag{S2}$$

We adopt the 1D heat equation for the subsurface,

$$\rho C_p \partial_t \theta_i \;=\; k \partial_z^2 \theta_i, \tag{S3}$$

where ρ is the material density, C_p is its heat capacity, θ_i is the depth dependent (z) temperature of facet i where surface temperature is denoted by $T_i = \theta_i$ (at $z = 0$), and finally k is the material conductivity. Solutions to Eq. S3 are developed in the time-asymptotic limit whereby we impose the condition that the conductive flux goes to zero sufficiently deep underneath the surface *(39)*. This amounts to representing the solution for the temperature for z < 0 as a truncated sum in powers of seasonal frequency, i.e.,

$$\begin{aligned} \theta_i \;&=\; \bar{T}_i + \sum_{n=1,N} \mathrm{e}^{\kappa_n z}\left(A_n \mathrm{e}^{i\omega_0 m t} + \text{c.c.}\right); \\ \kappa_n \;&\equiv\; (1+i)\sqrt{\frac{n\,\omega_0 \rho C_p}{2k}}; \end{aligned} \tag{S4}$$

where $\bar{T}_i$ is the local mean temperature of element i. This solution approach has also been used in the thermal response analysis of Martian sand dunes *(97)*. We construct solutions based on daily averaged solar insolation and proceed by building a received insolation profile for 298 evenly selected times over the course of ~298 year orbit of Arrokoth. We truncate the number of frequencies retained in Eq. S4 to about 75 so as to minimize the possibility of incurring de-aliasing errors in the solution procedure. We then build solutions to Eqs. S1 and S3 via an iterative procedure. We start by solving Eq. S1 for T_i with k set to zero and calculate a first iteration of Φ_i. This solution involves the inversion of a sparse matrix. This can be done via a forward iterative Gauss procedure because the matrix is well-conditioned. Then we correct T_i by solving Eq. S3 using this first guess for Φ_i, as the flux boundary condition $k\partial_z\theta_i|_{z=0} + \epsilon_i\sigma_B\theta_i^4|_{z=0} = \Phi_i$. This provides a corrected surface temperature $T_i = \theta_i|_{z=0}$ which is input back into Eq. S1 whereupon an updated value of Φ_i is assessed and used as an updated upper boundary condition used to solve Eq. S3. This iterates until a converged solution is reached which is usually assessed to be when the maximum change between successive iterations is sufficiently small, i.e., when $\max(\Delta\Phi_i/\Phi_i) < 10^{-4}$, where $\Delta\Phi_i$ is the difference between successive iterations of Φ_i.

Following *(1, 40)*, we assumed thermal inertia Γ = 2.5 J m^{-2} s$^{-1/2}$ K^{-1}. The resulting 16 K model mean surface temperature across the face of Arrokoth oriented toward New Horizons during the REX CA08 observation is far below the 29 ± 5 K brightness temperature recorded by REX. However, thermal radiation tends to emerge from a range of depths within a surface, potentially extending to many times the wavelength below the surface. Additionally, we do not know the X-band emissivity (ϵ) of Arrokoth's surface that provides the link between kinetic and brightness temperatures. To explore the range of parameters permitted by the REX observation, we re-ran our model with Γ ranging from 0.5 to 250 J m^{-2} s$^{-1/2}$ K^{-1} and computed temperatures at depths from the surface down to 4 m below the surface (~100 wavelengths), as shown in Fig. S1. The observed REX thermal emission is consistent with low thermal inertia and emission emerging from tens of cm below the surface, but is also consistent with higher thermal inertia and emission from closer to the surface. For instance, at the nominal 2.5 J m^{-2} s$^{-1/2}$ K^{-1} thermal inertia, the mean temperature over the observed hemisphere is 29 K at a mean depth of ~50 cm (12 REX wavelengths). For less than unit emissivity, warmer temperatures are needed to account for the observed T_B, consistent with emission from greater depths. With ϵ = 0.8, the corresponding kinetic temperature would be 36 K, which is reached at a depth of ~1 m. The maximum temperatures seen for any thermal inertia and depth combination are in the ~41 K range, implying a lower limit of 0.7 for the REX wavelength emissivity.

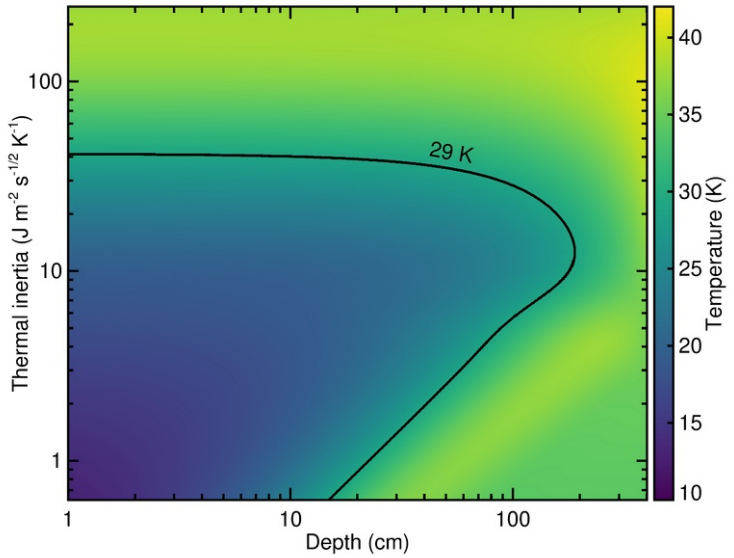

Figure S1. Model average temperature over the face of Arrokoth that was oriented toward New Horizons at the time of the REX CA08 scan, as a function of Γ and depth. Emission from the depth where T = 29 K (black curve) would be consistent with the REX measurement if ϵ = 1, but ϵ is likely to be smaller, so even warmer temperatures are likely required to account for the observed T_B.

For the higher thermal inertia solutions, the required value of Γ would be >40 J m^{-2} s$^{-1/2}$ K^{-1} to reconcile the surface temperature with the REX observation with unit emissivity at REX

wavelengths. Surface and subsurface temperatures are similar for the high thermal inertia models, so the higher thermal inertia models place less constraint on the depth sampled by the 4.2 cm the emission. A high thermal inertia is inconsistent with the statistical estimates from *(40)*, but those estimates are for diurnal timescales rather than seasonal timescales. Higher thermal conduction at depth could enable seasonal thermal inertias to be much higher than the values relevant for diurnal timescales. Additionally, the *(40)* sample does not include small CCKBOs in Arrokoth's size range, so it might not even be relevant to such objects.

Effects of unresolved surface roughness can be important in some thermal environments. These were explored by *(98)* through use of effective values of the albedo and emissivity. Arrokoth's bond albedo has been directly measured as 0.06 *(1, 3)*, so we leave it unchanged, but we tried higher values of emissivity $\epsilon = 0.95$ and $\epsilon = 1.0$ consistent with a rough surface. These led to slightly lower temperatures by up to 1 K across the observed face of Arrokoth, not enough to materially affect our conclusions.

Data S1 (separate file).

A low facet count version of the Arrokoth shape model *(3)* used in our themal models is provided as an ASCII file consisting of 1,039 lines representing vertices starting with the character v, followed by 1,962 lines representing facets starting with the character f. Each vertex line has three white-space separated floating point values representing *x, y, z* coordinates in units of km. The axes are aligned with the shape's principal axes of inertia and the origin corresponds to the center of mass assuming a uniform internal density. Each facet line has three white-space separated integers specifying three vertices to define the corners of that triangular facet, in order such that the right hand rule points in the direction of the exterior of the shape. The index of the first vertex line is 1 and the last is 1,039.

References

1. S. A. Stern, H. A. Weaver, J. R. Spencer, C. B. Olkin, G. R. Gladstone, W. M. Grundy, J. M. Moore, D. P. Cruikshank, H. A. Elliott, W. B. McKinnon, J. W. Parker, A. J. Verbiscer, L. A. Young, D. A. Aguilar, J. M. Albers, T. Andert, J. P. Andrews, F. Bagenal, M. E. Banks, B. A. Bauer, J. A. Bauman, K. E. Bechtold, C. B. Beddingfield, N. Behrooz, K. B. Beisser, S. D. Benecchi, E. Bernardoni, R. A. Beyer, S. Bhaskaran, C. J. Bierson, R. P. Binzel, E. M. Birath, M. K. Bird, D. R. Boone, A. F. Bowman, V. J. Bray, D. T. Britt, L. E. Brown, M. R. Buckley, M. W. Buie, B. J. Buratti, L. M. Burke, S. S. Bushman, B. Carcich, A. L. Chaikin, C. L. Chavez, A. F. Cheng, E. J. Colwell, S. J. Conard, M. P. Conner, C. A. Conrad, J. C. Cook, S. B. Cooper, O. S. Custodio, C. M. Dalle Ore, C. C. Deboy, P. Dharmavaram, R. D. Dhingra, G. F. Dunn, A. M. Earle, A. F. Egan, J. Eisig, M. R. El-Maarry, C. Engelbrecht, B. L. Enke, C. J. Ercol, E. D. Fattig, C. L. Ferrell, T. J. Finley, J. Firer, J. Fischetti, W. M. Folkner, M. N. Fosbury, G. H. Fountain, J. M. Freeze, L. Gabasova, L. S. Glaze, J. L. Green, G. A. Griffith, Y. Guo, M. Hahn, D. W. Hals, D. P. Hamilton, S. A. Hamilton, J. J. Hanley, A. Harch, K. A. Harmon, H. M. Hart, J. Hayes, C. B. Hersman, M. E. Hill, T. A. Hill, J. D. Hofgartner, M. E. Holdridge, M. Horányi, A. Hosadurga, A. D. Howard, C. J. A. Howett, S. E. Jaskulek, D. E. Jennings, J. R. Jensen, M. R. Jones, H. K. Kang, D. J. Katz, D. E. Kaufmann, J. J. Kavelaars, J. T. Keane, G. P. Keleher, M. Kinczyk, M. C. Kochte, P. Kollmann, S. M. Krimigis, G. L. Kruizinga, D. Y. Kusnierkiewicz, M. S. Lahr, T. R. Lauer, G. B. Lawrence, J. E. Lee, E. J. Lessac-Chenen, I. R. Linscott, C. M. Lisse, A. W. Lunsford, D. M. Mages, V. A. Mallder, N. P. Martin, B. H. May, D. J. McComas, R. L. McNutt Jr., D. S. Mehoke, T. S. Mehoke, D. S. Nelson, H. D. Nguyen, J. I. Núñez, A. C. Ocampo, W. M. Owen, G. K. Oxton, A. H. Parker, M. Pätzold, J. Y. Pelgrift, F. J. Pelletier, J. P. Pineau, M. R. Piquette, S. B. Porter, S. Protopapa, E. Quirico, J. A. Redfern, A. L. Regiec, H. J. Reitsema, D. C. Reuter, D. C. Richardson, J. E. Riedel, M. A. Ritterbush, S. J. Robbins, D. J. Rodgers, G. D. Rogers, D. M. Rose, P. E. Rosendall, K. D. Runyon, M. G. Ryschkewitsch, M. M. Saina, M. J. Salinas, P. M. Schenk, J. R. Scherrer, W. R. Schlei, B. Schmitt, D. J. Schultz, D. C. Schurr, F. Scipioni, R. L. Sepan, R. G. Shelton, M. R. Showalter, M. Simon, K. N. Singer, E. W. Stahlheber, D. R. Stanbridge, J. A. Stansberry, A. J. Steffl, D. F. Strobel, M. M. Stothoff, T. Stryk, J. R. Stuart, M. E. Summers, M. B. Tapley, A. Taylor, H. W. Taylor, R. M. Tedford, H. B. Throop, L. S. Turner, O. M. Umurhan, J. Van Eck, D. Velez, M. H. Versteeg, M. A. Vincent, R. W. Webbert, S. E. Weidner, G. E. Weigle 2nd, J. R. Wendel, O. L. White, K. E. Whittenburg, B. G. Williams, K. E. Williams, S. P. Williams, H. L. Winters, A. M. Zangari, T. H. Zurbuchen, Initial results from the New Horizons exploration of 2014 MU_{69}, a small Kuiper Belt object. *Science* **364**, eaaw9771 (2019). doi:10.1126/science.aaw9771 Medline

2. S. B. Porter, M. W. Buie, A. H. Parker, J. R. Spencer, S. Benecchi, P. Tanga, A. Verbiscer, J. J. Kavelaars, S. D. J. Gwyn, E. F. Young, H. A. Weaver, C. B. Olkin, J. W. Parker, S. A.

Stern, High-precision orbit fitting and uncertainty analysis of (486958) 2014 MU_{69}. *Astron. J.* **156**, 20 (2018). doi:10.3847/1538-3881/aac2e1

3. J. R. Spencer, S. A. Stern, J. M. Moore, H. A. Weaver, K. N. Singer, C. B. Olkin, A. J. Verbiscer, W. B. McKinnon, J. W. Parker, R. A. Beyer, J. T. Keane, T. R. Lauer, S. B. Porter, O. L. White, B. J. Buratti, M. R. El-Maarry, C. M. Lisse, A. H. Parker, H. B. Throop, S. J. Robbins, O. M. Umurhan, R. P. Binzel, D. T. Britt, M. W. Buie, A. F. Cheng, D. P. Cruikshank, H. A. Elliott, G. R. Gladstone, W. M. Grundy, M. E. Hill, M. Horányi, D. E. Jennings, J. J. Kavelaars, I. R. Linscott, D. J. McComas, R. L. McNutt Jr., S. Protopapa, D. C. Reuter, P. M. Schenk, M. R. Showalter, L. A. Young, A. M. Zangari, A. Y. Abedin, C. B. Beddingfield, S. D. Benecchi, E. Bernardoni, C. J. Bierson, D. Borncamp, V. J. Bray, A. L. Chaikin, R. D. Dhingra, C. Fuentes, T. Fuse, P. L. Gay, S. D. J. Gwyn, D. P. Hamilton, J. D. Hofgartner, M. J. Holman, A. D. Howard, C. J. A. Howett, H. Karoji, D. E. Kaufmann, M. Kinczyk, B. H. May, M. Mountain, M. Pätzold, J. M. Petit, M. R. Piquette, I. N. Reid, H. J. Reitsema, K. D. Runyon, S. S. Sheppard, J. A. Stansberry, T. Stryk, P. Tanga, D. J. Tholen, D. E. Trilling, L. H. Wasserman, The geology and geophysics of Kuiper Belt object (486958) Arrokoth. *Science* **367**, 10.1126/science.aay3999 (2020).

4. J.-M. Petit, J. J. Kavelaars, B. J. Gladman, R. L. Jones, J. W. Parker, C. Van Laerhoven, P. Nicholson, G. Mars, P. Rousselot, O. Mousis, B. Marsden, A. Bieryla, M. Taylor, M. L. N. Ashby, P. Benavidez, A. Campo Bagatin, G. Bernabeu, The Canada-France Ecliptic Plane Survey - full data release: The orbital structure of the Kuiper belt. *Astron. J.* **142**, 131 (2011). doi:10.1088/0004-6256/142/4/131

5. H. F. Levison, A. Morbidelli, C. Van Laerhoven, R. Gomes, K. Tsiganis, Origin of the structure of the Kuiper belt during a dynamical instability in the orbits of Uranus and Neptune. *Icarus* **196**, 258–273 (2008). doi:10.1016/j.icarus.2007.11.035

6. K. S. Noll, W. M. Grundy, D. C. Stephens, H. F. Levison, S. D. Kern, Evidence for two populations of classical transneptunian objects: The strong inclination dependence of classical binaries. *Icarus* **194**, 758–768 (2008). doi:10.1016/j.icarus.2007.10.022

7. S. C. Tegler, W. Romanishin, Extremely red Kuiper-belt objects in near-circular orbits beyond 40 AU. *Nature* **407**, 979–981 (2000). doi:10.1038/35039572 Medline

8. R. E. Pike, W. C. Fraser, M. E. Schwamb, J. J. Kavelaars, M. Marsset, M. T. Bannister, M. J. Lehner, S.-Y. Wang, M. Alexandersen, Y.-T. Chen, B. J. Gladman, S. Gwyn, J.-M. Petit, K. Volk, Col-OSSOS: Z-band photometry reveals three distinct TNO surface types. *Astron. J.* **154**, 101 (2017). doi:10.3847/1538-3881/aa83b1

9. H. F. Levison, S. A. Stern, On the size dependence of the inclination distribution of the main Kuiper Belt. *Astron. J.* **121**, 1730–1735 (2001). doi:10.1086/319420

10. M. E. Schwamb, M. E. Brown, W. C. Fraser, The small numbers of large Kuiper belt objects. *Astron. J.* **147**, 2 (2014). doi:10.1088/0004-6256/147/1/2

11. M. J. Brucker, W. M. Grundy, J. A. Stansberry, J. R. Spencer, S. S. Sheppard, E. I. Chiang, M. W. Buie, High albedos of low inclination Classical Kuiper belt objects. *Icarus* **201**, 284–294 (2009). doi:10.1016/j.icarus.2008.12.040

12. E. Vilenius, C. Kiss, T. Müller, M. Mommert, P. Santos-Sanz, A. Pál, J. Stansberry, M. Mueller, N. Peixinho, E. Lellouch, S. Fornasier, A. Delsanti, A. Thirouin, J. L. Ortiz, R. Duffard, D. Perna, F. Henry, "TNOs are Cool": A survey of the trans-neptunian region X. Analysis of classical Kuiper belt objects from Herschel and Spitzer observations. *Astron. Astrophys.* **564**, A35 (2014). doi:10.1051/0004-6361/201322416

13. W. B. McKinnon, D. C. Richardson, J. C. Marohnic, J. T. Keane, W. M. Grundy, D. P. Hamilton, D. Nesvorný, O. M. Umurhan, T. R. Lauer, K. N. Singer, S. A. Stern, H. A. Weaver, J. R. Spencer, M. W. Buie, J. M. Moore, J. J. Kavelaars, C. M. Lisse, X. Mao, A. H. Parker, S. B. Porter, M. R. Showalter, C. B. Olkin, D. P. Cruikshank, H. A. Elliott, G. R. Gladstone, J. W. Parker, A. J. Verbiscer, L. A. Young, New Horizons Science Team, The solar nebula origin of (486958) Arrokoth, a primordial contact binary in the Kuiper Belt. *Science* **367**, 10.1126/science.aay6620 (2020).

14. D. C. Reuter, S. A. Stern, J. Scherrer, D. E. Jennings, J. W. Baer, J. Hanley, L. Hardaway, A. Lunsford, S. McMuldroch, J. Moore, C. Olkin, R. Parizek, H. Reitsma, D. Sabatke, J. Spencer, J. Stone, H. Throop, J. Van Cleve, G. E. Weigle, L. A. Young, Ralph: A visible/infrared imager for the New Horizons Pluto/Kuiper belt mission. *Space Sci. Rev.* **140**, 129–154 (2008). doi:10.1007/s11214-008-9375-7

15. See supplementary materials.

16. A. F. Cheng, H. A. Weaver, S. J. Conard, M. F. Morgan, O. Barnouin-Jha, J. D. Boldt, K. A. Cooper, E. H. Darlington, M. P. Grey, J. R. Hayes, K. E. Kosakowski, T. Magee, E. Rossano, D. Sampath, C. Schlemm, H. W. Taylor, Long-Range Reconnaissance Imager on New Horizons. *Space Sci. Rev.* **140**, 189–215 (2008). doi:10.1007/s11214-007-9271-6

17. G. L. Tyler, I. R. Linscott, M. K. Bird, D. P. Hinson, D. F. Strobel, M. Pätzold, M. E. Summers, K. Sivaramakrishnan, The New Horizons radio science experiment (REX). *Space Sci. Rev.* **140**, 217–259 (2008). doi:10.1007/s11214-007-9302-3

18. O. R. Hainaut, A. C. Delsanti, Colors of minor bodies in the outer Solar System: A statistical analysis. *Astron. Astrophys.* **389**, 641–664 (2002). doi:10.1051/0004-6361:20020431

19. D. P. Cruikshank, H. Imanaka, C. M. Dalle Ore, Tholins as coloring agents on outer Solar System bodies. *Adv. Space Res.* **36**, 178–183 (2005). doi:10.1016/j.asr.2005.07.026

20. B. N. Khare, C. Sagan, E. T. Arakawa, F. Suits, T. A. Callcott, M. W. Williams, Optical constants of organic tholins produced in a simulated Titanian atmosphere: From soft X-

ray to microwave frequencies. *Icarus* **60**, 127–134 (1984). doi:10.1016/0019-1035(84)90142-8

21. B. N. Khare, W. R. Thompson, L. Cheng, C. Chyba, C. Sagan, E. T. Arakawa, C. Meisse, P. S. Tuminello, Production and optical constants of ice tholin from charged particle irradiation of (1:6) C_2H_6/H_2O at 77 K. *Icarus* **103**, 290–300 (1993). doi:10.1006/icar.1993.1071

22. B. N. Khare *et al*., Optical constants of Triton tholin: Prelimary results. *Bull. Am. Astron. Soc.* **26**, 1176–1177 (1994).

23. H. Imanaka, B. N. Khare, J. E. Elsila, E. L. O. Bakes, C. P. McKay, D. P. Cruikshank, S. Sugita, T. Matsui, R. N. Zare, Laboratory experiments of Titan tholin formed in cold plasma at various pressures: Implications for nitrogen-containing polycyclic aromatic compounds in Titan haze. *Icarus* **168**, 344–366 (2004). doi:10.1016/j.icarus.2003.12.014

24. C. K. Materese, D. P. Cruikshank, S. A. Sandford, H. Imanaka, M. Nuevo, D. W. White, Ice chemistry on outer Solar System bodies: Carboxylic acids, nitriles, and urea detected in refractory residues produced from the UV photolysis of N_2:CH_4:CO-containing ices. *Astrophys. J.* **788**, 111 (2014). doi:10.1088/0004-637X/788/2/111

25. C. K. Materese, D. P. Cruikshank, S. A. Sandford, H. Imanaka, M. Nuevo, Ice chemistry on outer Solar System bodies: Electron radiolysis of N_2-, CH_4-, and CO-containing ices. *Astrophys. J.* **812**, 150 (2015). doi:10.1088/0004-637X/812/2/150

26. N. Peixinho, A. Delsanti, A. Guilbert-Lepoutre, R. Gafeira, P. Lacerda, The bimodal colors of Centaurs and small Kuiper belt objects. *Astron. Astrophys.* **546**, A86 (2012). doi:10.1051/0004-6361/201219057

27. F. E. DeMeo, B. Carry, The taxonomic distribution of asteroids from multi-filter all-sky photometric surveys. *Icarus* **226**, 723–741 (2013). doi:10.1016/j.icarus.2013.06.027

28. G. M. Szabó, Z. Ivezić, M. Jurić, R. Lupton, The properties of jovian Trojan asteroids listed in SDSS Moving Object Catalogue 3. *Mon. Not. R. Astron. Soc.* **377**, 1393–1406 (2007). doi:10.1111/j.1365-2966.2007.11687.x

29. W. C. Fraser, M. E. Brown, The Hubble Wide Field Camera 3 test of surfaces in the outer Solar System: The compositional classes of the Kuiper belt. *Astrophys. J.* **749**, 33 (2012). doi:10.1088/0004-637X/749/1/33

30. B. Schmitt, S. Philippe, W. M. Grundy, D. C. Reuter, R. Côte, E. Quirico, S. Protopapa, L. A. Young, R. P. Binzel, J. C. Cook, D. P. Cruikshank, C. M. Dalle Ore, A. M. Earle, K. Ennico, C. J. A. Howett, D. E. Jennings, I. R. Linscott, A. W. Lunsford, C. B. Olkin, A. H. Parker, J. W. Parker, K. N. Singer, J. R. Spencer, J. A. Stansberry, S. A. Stern, C. C. C. Tsang, A. J. Verbiscer, H. A. Weaver, Physical state and distribution of materials at the surface of Pluto from New Horizons LEISA imaging spectrometer. *Icarus* **287**, 229–260 (2017). doi:10.1016/j.icarus.2016.12.025

31. B. Hapke, *Theory of Reflectance and Emittance Spectroscopy* (Cambridge Univ. Press, ed. 2, 2012).

32. S. A. Sandford, L. J. Allamandola, Condensation and vaporization studies of CH_3OH and NH_3 ices: Major implications for astrochemistry. *Astrophys. J.* **417**, 815–825 (1993). doi:10.1086/173362 Medline

33. D. P. Cruikshank, T. L. Roush, M. J. Bartholomew, T. R. Geballe, Y. J. Pendleton, S. M. White, J. F. Bell III, J. K. Davies, T. C. Owen, C. de Bergh, D. J. Tholen, M. P. Bernstein, R. H. Brown, K. A. Tryka, C. M. Dalle Ore, The composition of Centaur 5145 Pholus. *Icarus* **135**, 389–407 (1998). doi:10.1006/icar.1998.5997

34. M. A. Barucci, F. Merlin, E. Dotto, A. Doressoundiram, C. de Bergh, TNO surface ices: Observations of the TNO 55638 (2002 VE_{95}) and analysis of the population's spectral properties. *Astron. Astrophys.* **455**, 725–730 (2006). doi:10.1051/0004-6361:20064951

35. H. Zheng, M. Tegmark, J. S. Dillon, D. A. Kim, A. Liu, A. R. Neben, J. Jonas, P. Reich, W. Reich, An improved model of diffuse galactic radio emission from 10 MHz to 5 THz. *Mon. Not. R. Astron. Soc.* **464**, 3486–3497 (2017). doi:10.1093/mnras/stw2525

36. M. K. Bird, I. R. Linscott, G. L. Tyler, D. P. Hinson, M. Pätzold, M. E. Summers, D. F. Strobel, S. A. Stern, H. A. Weaver, C. B. Olkin, L. A. Young, K. Ennico, J. M. Moore, G. R. Gladstone, W. M. Grundy, C. C. DeBoy, M. Vincent, Radio thermal emission from Pluto and Charon during the New Horizons encounter. *Icarus* **322**, 192–209 (2019). doi:10.1016/j.icarus.2019.01.004

37. I. R. Linscott *et al*., Radiometer Calibration at 4.2 cm on New Horizons. Stanford Radioscience Report No. 17-06-0 (2017); https://sbn.astro.umd.edu/holdings/nh-j-rex-2-jupiter-v2.0/document/nh_rex_radiometer_calib_v4p7.pdf.

38. D. Vokrouhlický, W. F. Bottke, S. R. Chesley, D. J. Scheeres, T. S. Statler, in *Asteroids IV*, P. Michel, F. E. DeMeo, W. F. Bottke, Eds. (Univ. of Arizona Press, 2015), pp. 509–531.

39. O. L. White, O. M. Umurhan, J. W. Moore, A. D. Howard, Modeling of ice pinnacle formation on Callisto. *J. Geophys. Res.* **121**, 21–45 (2016). doi:10.1002/2015JE004846

40. E. Lellouch, P. Santos-Sanz, P. Lacerda, M. Mommert, R. Duffard, J. L. Ortiz, T. G. Müller, S. Fornasier, J. Stansberry, C. Kiss, E. Vilenius, M. Mueller, N. Peixinho, R. Moreno, O. Groussin, A. Delsanti, A. W. Harris, "TNOs are Cool": A survey of the trans-neptunian region IX. Thermal properties of Kuiper belt objects and Centaurs from combined Herschel and Spitzer observations. *Astron. Astrophys.* **557**, A60 (2013). doi:10.1051/0004-6361/201322047

41. M. Pätzold, T. Andert, M. Hahn, S. W. Asmar, J.-P. Barriot, M. K. Bird, B. Häusler, K. Peter, S. Tellmann, E. Grün, P. R. Weissman, H. Sierks, L. Jorda, R. Gaskell, F. Preusker, F. Scholten, A homogeneous nucleus for comet 67P/Churyumov-Gerasimenko from its gravity field. *Nature* **530**, 63–65 (2016). doi:10.1038/nature16535 Medline

42. C. J. Bierson, F. Nimmo, Using the density of Kuiper belt objects to constrain their composition and formation history. *Icarus* **326**, 10–17 (2019). doi:10.1016/j.icarus.2019.01.027

43. J. R. Spencer, A rough-surface thermophysical model for airless planets. *Icarus* **83**, 27–38 (1990). doi:10.1016/0019-1035(90)90004-S

44. R. S. Gomes, A. Morbidelli, H. F. Levison, Planetary migration in a planetesimal disk: Why did Neptune stop at 30 au. *Icarus* **170**, 492–507 (2004). doi:10.1016/j.icarus.2004.03.011

45. A. Shannon, Y. Wu, Y. Lithwick, Forming the cold classical Kuiper belt in a light disk. *Astrophys. J.* **818**, 175 (2016). doi:10.3847/0004-637X/818/2/175

46. K. M. Barkume, M. E. Brown, E. L. Schaller, Near-infrared spectra of Centaurs and Kuiper belt objects. *Astron. J.* **135**, 55–67 (2008). doi:10.1088/0004-6256/135/1/55

47. M. A. Barucci, A. Alvarez-Candal, F. Merlin, I. N. Belskaya, C. de Bergh, D. Perna, F. DeMeo, S. Fornasier, New insights on ices in Centaur and transneptunian populations. *Icarus* **214**, 297–307 (2011). doi:10.1016/j.icarus.2011.04.019

48. D. Nesvorný, R. Li, A. Youdin, J. B. Simon, W. M. Grundy, Trans-Neptunian binaries as evidence for planetesimal formation by the streaming instability. *Nat. Astron.* **3**, 808–812 (2019). doi:10.1038/s41550-019-0806-z

49. C. Dominik, A. G. G. M. Tielens, The physics of dust coagulation and the structure of dust aggregates in space. *Astrophys. J.* **480**, 647–673 (1997). doi:10.1086/303996

50. J. Blum, G. Wurm, The growth mechanisms of macroscopic bodies in protoplanetary disks. *Annu. Rev. Astron. Astrophys.* **46**, 21–56 (2008). doi:10.1146/annurev.astro.46.060407.145152

51. A. N. Youdin, J. Goodman, Streaming instabilities in protoplanetary disks. *Astrophys. J.* **620**, 459–469 (2005). doi:10.1086/426895

52. A. Johansen, J. S. Oishi, M. M. Mac Low, H. Klahr, T. Henning, A. Youdin, Rapid planetesimal formation in turbulent circumstellar disks. *Nature* **448**, 1022–1025 (2007). doi:10.1038/nature06086 Medline

53. S. J. Weidenschilling, Aerodynamics of solid bodies in the solar nebula. *Mon. Not. R. Astron. Soc.* **180**, 57–70 (1977). doi:10.1093/mnras/180.2.57

54. M. N. Drozdovskaya, C. Walsh, E. F. van Dishoeck, K. Furuya, U. Marboeuf, A. Thiabaud, D. Harsono, R. Visser, Cometary ices in forming protoplanetary disc midplanes. *Mon. Not. R. Astron. Soc.* **462**, 977–993 (2016). doi:10.1093/mnras/stw1632

55. T. Henning, D. Semenov, Chemistry in protoplanetary disks. *Chem. Rev.* **113**, 9016–9042 (2013). doi:10.1021/cr400128p Medline

56. F. J. Ciesla, S. A. Sandford, Organic synthesis via irradiation and warming of ice grains in the solar nebula. *Science* **336**, 452–454 (2012). doi:10.1126/science.1217291 Medline

57. K. I. Öberg, R. Murray-Clay, E. A. Bergin, The effect of snowlines on C/O in planetary atmospheres. *Astrophys. J.* **743**, L16 (2011). doi:10.1088/2041-8205/743/1/L16

58. A. G. G. M. Tielens, W. Hagen, Model calculations of the molecular composition of interstellar grain mantles. *Astron. Astrophys.* **114**, 245–260 (1982).

59. H. M. Cuppen, E. F. van Dishoeck, E. Herbst, A. G. G. M. Tielens, Microscopic simulation of methanol and formaldehyde ice formation in cold dense cores. *Astron. Astrophys.* **508**, 275–287 (2009). doi:10.1051/0004-6361/200913119

60. M. Ruaud, U. Gorti, A three-phase approach to grain surface chemistry in protoplanetary disks: Gas, ice surfaces, and ice mantles of dust grains. *Astrophys. J.* **885**, 146 (2019). doi:10.3847/1538-4357/ab4996

61. A. D. Bosman, C. Walsh, E. F. van Dishoeck, CO destruction in protoplanetary disk midplanes: Inside versus outside the CO snow surface. *Astron. Astrophys.* **618**, A182 (2018). doi:10.1051/0004-6361/201833497

62. R. Brunetto, G. A. Baratta, M. Domingo, G. Strazzulla, Reflectance and transmittance spectra (2.2-2.4 μm) of ion irradiated methanol. *Icarus* **175**, 226–232 (2005). doi:10.1016/j.icarus.2004.10.011

63. M. H. Moore, R. L. Hudson, Infrared study of ion-irradiated water-ice mixtures with hydrocarbons relevant to comets. *Icarus* **135**, 518–527 (1998). doi:10.1006/icar.1998.5996

64. A. Wada, N. Mochizuki, K. Hiraoka, Methanol formation from electron-irradiated mixed H_2O/CH_4 ice at 10 K. *Astrophys. J.* **644**, 300–306 (2006). doi:10.1086/503380

65. R. Hodyss, P. V. Johnson, J. V. Stern, J. D. Goguen, I. Kanik, Photochemistry of methane–water ices. *Icarus* **200**, 338–342 (2009). doi:10.1016/j.icarus.2008.10.024

66. M. P. Pearce, M. J. Bussemaker, P. D. Cooper, K. M. Lapere, D. A. Wild, A. J. McKinley, Formation of methanol from methane and water in an electrical discharge. *Phys. Chem. Chem. Phys.* **14**, 3444–3449 (2012). doi:10.1039/c2cp22135g Medline

67. G. D. McDonald, L. J. Whited, C. DeRuiter, B. N. Khare, A. Patnaik, C. Sagan, Production and chemical analysis of cometary ice tholins. *Icarus* **122**, 107–117 (1996). doi:10.1006/icar.1996.0112

68. C. Walsh, R. A. Loomis, K. I. Öberg, M. Kama, M. L. R. van ’t Hoff, T. J. Millar, Y. Aikawa, E. Herbst, S. L. Widicus Weaver, H. Nomura, First detection of gas-phase methanol in a protoplanetary disk. *Astrophys. J.* **823**, L10 (2016). doi:10.3847/2041-8205/823/1/L10

69. C. Walsh, S. Vissapragada, H. McGee, in *Astrochemistry VII - Through the Cosmos from Galaxies to Planets, Proceedings IAU Symposium No. 332*, M. Cunningham, T. Millar, Y. Aikawa, Eds. (International Astronomical Union, 2018), pp. 395–402.

70. E. A. Bergin, L. I. Cleeves, U. Gorti, K. Zhang, G. A. Blake, J. D. Green, S. M. Andrews, N. J. Evans 2nd, T. Henning, K. Öberg, K. Pontoppidan, C. Qi, C. Salyk, E. F. van Dishoeck, An old disk still capable of forming a planetary system. *Nature* **493**, 644–646 (2013). doi:10.1038/nature11805 Medline

71. M. K. McClure, E. A. Bergin, L. I. Cleeves, E. F. Dishoeck, G. A. Blake, N. J. Evans II, J. D. Green, T. Henning, K. I. Öberg, K. M. Pontoppidan, C. Salyk, Mass measurements in protoplanetary disks from hydrogen deuteride. *Astrophys. J.* **831**, 167 (2016). doi:10.3847/0004-637X/831/2/167

72. S. Krijt, K. R. Schwarz, E. A. Bergin, F. J. Ciesla, Transport of CO in protoplanetary disks: Consequences of pebble formation, settling, and radial drift. *Astrophys. J.* **864**, 78 (2018). doi:10.3847/1538-4357/aad69b

73. K. Zhang, E. A. Bergin, K. Schwarz, S. Krijt, F. Ciesla, Systematic variations of CO gas abundance with radius in gas-rich protoplanetary disks. *Astrophys. J.* **883**, 98 (2019). doi:10.3847/1538-4357/ab38b9

74. S. C. Tegler, W. Romanishin, G. J. Consolmagno, J. Rall, R. Worhatch, M. Nelson, S. Weidenschilling, The period of rotation, shape, density, and homogeneous surface color of the Centaur 5145 Pholus. *Icarus* **175**, 390–396 (2005). doi:10.1016/j.icarus.2004.12.011

75. M. A. Barucci, F. Merlin, D. Perna, A. Alvarez-Candal, T. Müller, M. Mommert, C. Kiss, S. Fornasier, P. Santos-Sanz, E. Dotto, The extra red plutino (55638) 2002 VE_{95}. *Astron. Astrophys.* **539**, A152 (2012). doi:10.1051/0004-6361/201118505

76. M. P. Bernstein, S. A. Sandford, L. J. Allamandola, S. Chang, M. A. Scharberg, Organic compounds produced by photolysis of realistic interstellar and cometary ice analogs containing methanol. *Astrophys. J.* **454**, 327–344 (1995). doi:10.1086/176485

77. T. Butscher, F. Duvernay, G. Danger, R. Torro, G. Lucas, Y. Carissan, D. Hagebaum-Reignier, T. Chiavassa, Radical-assisted polymerization in interstellar ice analogues: Formyl radical and polyoxymethylene. *Mon. Not. R. Astron. Soc.* **486**, 1953–1963 (2019). doi:10.1093/mnras/stz879

78. M. Piquette, A. R. Poppe, E. Bernardoni, J. R. Szalay, D. James, M. Horányi, S. A. Stern, H. Weaver, J. Spencer, C. Olkin, Student Dust Counter: Status report at 38 au. *Icarus* **321**, 116–125 (2019). doi:10.1016/j.icarus.2018.11.012

79. A. R. Poppe, C. M. Lisse, M. Piquette, M. Zemcov, M. Horányi, D. James, J. R. Szalay, E. Bernardoni, S. A. Stern, Constraining the Solar System's debris disk with in situ New

Horizons measurements from the Edgeworth-Kuiper belt. *Astrophys. J.* **881**, L12 (2019). doi:10.3847/2041-8213/ab322a

80. S. A. Stern, ISM-induced erosion and gas-dynamical drag in the Oort cloud. *Icarus* **84**, 447–466 (1990). doi:10.1016/0019-1035(90)90048-E

81. S. A. Stern, The evolution of comets in the Oort cloud and Kuiper belt. *Nature* **424**, 639–642 (2003). doi:10.1038/nature01725 Medline

82. S. D. Benecchi, K. S. Noll, W. M. Grundy, M. W. Buie, D. C. Stephens, H. F. Levison, The correlated colors of transneptunian binaries. *Icarus* **200**, 292–303 (2009). doi:10.1016/j.icarus.2008.10.025

83. O. Mousis, A. Guilbert-Lepoutre, B. Brugger, L. Jorda, J. S. Kargel, A. Bouquet, A.-T. Auger, P. Lamy, P. Vernazza, N. Thomas, H. Sierks, Pits formation from volatile outgassing on 67P/Churyumov-Gerasimenko. *Astrophys. J.* **814**, L5 (2015). doi:10.1088/2041-8205/814/1/L5

84. J. B. Vincent, D. Bodewits, S. Besse, H. Sierks, C. Barbieri, P. Lamy, R. Rodrigo, D. Koschny, H. Rickman, H. U. Keller, J. Agarwal, M. F. A'Hearn, A.-T. Auger, M. A. Barucci, J.-L. Bertaux, I. Bertini, C. Capanna, G. Cremonese, V. Da Deppo, B. Davidsson, S. Debei, M. De Cecco, M. R. El-Maarry, F. Ferri, S. Fornasier, M. Fulle, R. Gaskell, L. Giacomini, O. Groussin, A. Guilbert-Lepoutre, P. Gutierrez-Marques, P. J. Gutiérrez, C. Güttler, N. Hoekzema, S. Höfner, S. F. Hviid, W.-H. Ip, L. Jorda, J. Knollenberg, G. Kovacs, R. Kramm, E. Kührt, M. Küppers, F. La Forgia, L. M. Lara, M. Lazzarin, V. Lee, C. Leyrat, Z.-Y. Lin, J. J. Lopez Moreno, S. Lowry, S. Magrin, L. Maquet, S. Marchi, F. Marzari, M. Massironi, H. Michalik, R. Moissl, S. Mottola, G. Naletto, N. Oklay, M. Pajola, F. Preusker, F. Scholten, N. Thomas, I. Toth, C. Tubiana, Large heterogeneities in comet 67P as revealed by active pits from sinkhole collapse. *Nature* **523**, 63–66 (2015). doi:10.1038/nature14564 Medline

85. P. Ayotte, R. S. Smith, K. P. Stevenson, Z. Dohnálek, G. A. Kimmel, B. D. Kay, Effect of porosity on the adsorption, desorption, trapping, and release of volatile gases by amorphous solid water. *J. Geophys. Res.* **106**, 33387–33392 (2001). doi:10.1029/2000JE001362

86. A. Bar-Nun, G. Notesco, T. Owen, Trapping of N_2, CO and Ar in amorphous ice: Application to comets. *Icarus* **190**, 655–659 (2007). doi:10.1016/j.icarus.2007.03.021

87. M. Massironi, E. Simioni, F. Marzari, G. Cremonese, L. Giacomini, M. Pajola, L. Jorda, G. Naletto, S. Lowry, M. R. El-Maarry, F. Preusker, F. Scholten, H. Sierks, C. Barbieri, P. Lamy, R. Rodrigo, D. Koschny, H. Rickman, H. U. Keller, M. F. A'Hearn, J. Agarwal, A.-T. Auger, M. A. Barucci, J.-L. Bertaux, I. Bertini, S. Besse, D. Bodewits, C. Capanna, V. Da Deppo, B. Davidsson, S. Debei, M. De Cecco, F. Ferri, S. Fornasier, M. Fulle, R. Gaskell, O. Groussin, P. J. Gutiérrez, C. Güttler, S. F. Hviid, W.-H. Ip, J. Knollenberg, G.

Kovacs, R. Kramm, E. Kührt, M. Küppers, F. La Forgia, L. M. Lara, M. Lazzarin, Z.-Y. Lin, J. J. Lopez Moreno, S. Magrin, H. Michalik, S. Mottola, N. Oklay, A. Pommerol, N. Thomas, C. Tubiana, J.-B. Vincent, Two independent and primitive envelopes of the bilobate nucleus of comet 67P. *Nature* **526**, 402–405 (2015). doi:10.1038/nature15511 Medline

88. L. Penasa, M. Massironi, G. Naletto, E. Simioni, S. Ferrari, M. Pajola, A. Lucchetti, F. Preusker, F. Scholten, L. Jorda, R. Gaskell, F. Ferri, F. Marzari, B. Davidsson, S. Mottola, H. Sierks, C. Barbieri, P. L. Lamy, R. Rodrigo, D. Koschny, H. Rickman, H. U. Keller, J. Agarwal, M. F. A'Hearn, M. A. Barucci, J. L. Bertaux, I. Bertini, G. Cremonese, V. Da Deppo, S. Debei, M. De Cecco, J. Deller, C. Feller, S. Fornasier, E. Frattin, M. Fulle, O. Groussin, P. J. Gutierrez, C. Güttler, M. Hofmann, S. F. Hviid, W. H. Ip, J. Knollenberg, J. R. Kramm, E. Kührt, M. Küppers, F. La Forgia, L. M. Lara, M. Lazzarin, J.-C. Lee, J. J. Lopez Moreno, N. Oklay, X. Shi, N. Thomas, C. Tubiana, J. B. Vincent, A three-dimensional modelling of the layered structure of comet 67P/Churyumov-Gerasimenko. *Mon. Not. R. Astron. Soc.* **469** (suppl. 2), S741–S754 (2017). doi:10.1093/mnras/stx2899

89. C. J. A. Howett, A. H. Parker, C. B. Olkin, D. C. Reuter, K. Ennico, W. M. Grundy, A. L. Graps, K. P. Harrison, H. B. Throop, M. W. Buie, J. R. Lovering, S. B. Porter, H. A. Weaver, L. A. Young, S. A. Stern, R. A. Beyer, R. P. Binzel, B. J. Buratti, A. F. Cheng, J. C. Cook, D. P. Cruikshank, C. M. Dalle Ore, A. M. Earle, D. E. Jennings, I. R. Linscott, A. W. Lunsford, J. W. Parker, S. Phillippe, S. Protopapa, E. Quirico, P. M. Schenk, B. Schmitt, K. N. Singer, J. R. Spencer, J. A. Stansberry, C. C. C. Tsang, G. E. Weigle II, A. J. Verbiscer, Inflight radiometric calibration of New Horizons' Multispectral Visible Imaging Camera (MVIC). *Icarus* **287**, 140–151 (2017). doi:10.1016/j.icarus.2016.12.007

90. C. M. Dalle Ore, S. Protopapa, J. C. Cook, W. M. Grundy, D. P. Cruikshank, A. J. Verbiscer, K. Ennico, C. B. Olkin, S. A. Stern, H. A. Weaver, L. A. Young, Ices on Charon: Distribution of H_2O and NH_3 from New Horizons LEISA observations. *Icarus* **300**, 21–32 (2018). doi:10.1016/j.icarus.2017.08.026

91. C. H. Acton Jr., Ancillary data services of NASA's Navigation and Ancillary Information Facility. *Planet. Space Sci.* **44**, 65–70 (1996). doi:10.1016/0032-0633(95)00107-7

92. J. C. Cook, C. M. Dalle Ore, S. Protopapa, R. P. Binzel, D. P. Cruikshank, A. Earle, W. M. Grundy, K. Ennico, C. Howett, D. E. Jennings, A. W. Lunsford, C. B. Olkin, A. H. Parker, S. Philippe, D. Reuter, B. Schmitt, K. Singer, J. A. Stansberry, S. A. Stern, A. Verbiscer, H. A. Weaver, L. A. Young, J. Hanley, F. Alketbi, G. L. Thompson, L. A. Pearce, G. E. Lindberg, S. C. Tegler, The distribution of H_2O, CH_3OH, and hydrocarbon-ices on Pluto: Analysis of New Horizons spectral images. *Icarus* **331**, 148–169 (2019). doi:10.1016/j.icarus.2018.09.012

93. A. F. McGuire, B. W. Hapke, An experimental study of light scattering by large, irregular particles. *Icarus* **113**, 134–155 (1995). doi:10.1006/icar.1995.1012

94. F. Rouleau, P. G. Martin, Shape and clustering effects on the optical properties of amorphous carbon. *Astrophys. J.* **377**, 526–540 (1991). doi:10.1086/170382

95. W. M. Grundy, B. Schmitt, The temperature-dependent near-infrared absorption spectrum of hexagonal H_2O ice. *J. Geophys. Res.* **103**, 25809–25822 (1998). doi:10.1029/98JE00738

96. A. Zanchet, Y. Rodríguez-Lazcano, Ó. Gálvez, V. J. Herrero, R. Escribano, B. Maté, Optical constants of NH_3 and NH_3:N_2 amorphous ices in the near-infrared and mid-infrared regions. *Astrophys. J.* **777**, 26 (2013). doi:10.1088/0004-637X/777/1/26

97. T. N. Titus, G. E. Cushing, Thermal diffusivity experiment at the Grand Falls dune field. Third International Planetary Dunes Workshop, 12 to 15 June 2012, Flagstaff, AZ. LPI Contribution No. 7044.

98. A. P. Ingersoll, T. Svitek, B. C. Murray, Stability of polar frosts in spherical bowl-shaped craters on the moon, Mercury, and Mars. *Icarus* **100**, 40–47 (1992). doi:10.1016/0019-1035(92)90016-Z